



1 Water chemistry and greenhouse gas concentrations in waterbodies of a thawing permafrost
2 peatland complex in northern Norway

3 Jacqueline K. Knutson¹, François Clayer¹, Peter Dörsch^{2,3}, Sebastian Westermann^{2,4}, Heleen
4 A. de Wit^{1,2}.

5 1 Norwegian Institute for Water Research, Økernveien 94, 0579, Oslo, Norway

6 2 Centre for Biogeochemistry in the Anthropocene, University of Oslo, Oslo, 0371, Norway

7 3 Faculty of Environmental Sciences and Natural Resource Management, Norwegian

8 University of Life Sciences (NMBU), 1433 Ås, Norway

9 4 Department of Geosciences, University of Oslo, Oslo, 0371, Norway

10

11 Correspondence: Jacqueline K. Knutson (jacqueline.knutson@niva.no)



12 Abstract

13 Thermokarst ponds in thawing permafrost landscapes play a considerable role in greenhouse
14 gas (GHG) emissions despite their small size, yet they remain underrepresented in Earth
15 system models. At the Iškoras site in northern Norway, a peat plateau with decaying
16 permafrost and thermokarst ponds adjacent to a wetland, we studied water chemistry,
17 dissolved organic matter (DOM) processing, and GHG fluxes over two years. Thermokarst
18 ponds exhibited low pH, high organic acidity, and high oversaturation of dissolved carbon
19 dioxide (CO₂) and especially high dissolved methane (CH₄). Adjacent wetland streams,
20 however, with near-neutral pH, showed lower CH₄ and organic acidity but significantly
21 higher CO₂ emissions despite moderate saturations driven by turbulence and bicarbonate
22 replenishment. By contrast, CO₂ emissions in ponds were primarily linked to DOM
23 mineralization.

24 DOM mineralization rates were similar between ponds and streams, suggesting that
25 environmental factors like pH and microbial community differences counteract DOM lability
26 variations. As permafrost decays and transitions from peat plateaus to wetlands, ponds as
27 hotspots of CH₄ emissions will disappear. However, total GHG fluxes across the peatland-
28 wetland continuum will depend on wetland emissions, where CH₄ emissions usually are
29 considerable, and the fate of organic matter within the plateau. Lateral DOC fluxes may
30 represent a significant loss of soil organic carbon, highlighting the importance of
31 hydrological connectivity in linking terrestrial and aquatic systems. This study emphasizes
32 the need to account for the relationship between hydrological and chemical processes when
33 assessing C and GHG fluxes in permafrost-impacted regions.



34 1. Introduction

35 Northern latitude regions, which store approximately 1,300 Pg of organic carbon (OC)
36 (Hugelius et al., 2014), represent one of the largest terrestrial carbon reservoirs on Earth
37 (Schuur et al., 2008; Schuur et al., 2015; Walter et al., 2006). Sequestered under cold and
38 oxygen-limited conditions, this carbon (C) is increasingly vulnerable to release as permafrost
39 thaws due to climate warming, generating significant feedbacks that complicate predictions
40 of future climate trajectories (Schuur et al., 2008; Schuur et al., 2015; Walter et al., 2006). As
41 permafrost degrades, the release of greenhouse gases, particularly methane (CH₄) and carbon
42 dioxide (CO₂), through the microbial decomposition of previously frozen organic matter
43 (OM) can rapidly escalate the impact of this feedback (Schuur et al., 2008; Walter et al.,
44 2008; Wik et al., 2016; Zimov et al., 2006). While the large-scale thaw of permafrost is
45 widely recognized (Leppiniemi et al., 2023), the timing, magnitude, and pathways of carbon
46 release remain uncertain, influenced by processes such as burial, mobilization, lateral export,
47 and mineralization (Verdonen et al., 2023; Vonk et al., 2015).

48 Permafrost thaw leads to irreversible landscape transformations. Peatlands in northern
49 Norway are predominantly located in the sporadic permafrost zone, where they form
50 distinctive landscape features such as peat plateaus and palsas. These are peat uplands and
51 mounds with a frozen core, elevated above the water table by the formation of segregation ice
52 (Alewell et al., 2011; Krüger et al., 2017). As these features degrade, permafrost thaw is often
53 abrupt and subsidence and collapse is to be expected, leading to the formation thermokarst
54 ponds, as excess ground ice is lost (Martin et al., 2021). More than half of the permafrost
55 areas in the Scandinavian Peninsula are at risk of disappearing under current and projected
56 climate conditions (Gisnås et al., 2017; Schuur et al., 2008). The areal extent of peat plateaus
57 in this region decreased by 33%–71% between the 1950s and the 2010s, with rapid
58 degradation observed during the last decade (Borge et al., 2017). This regional degradation



59 mirrors processes observed across the northern hemisphere, including in the Canadian Arctic,
60 European Russia, and the Kola Peninsula, highlighting the vulnerability of sporadic
61 permafrost regions to warming climates (Krutskikh et al., 2023; Payette et al., 2004; Sannel
62 and Kuhry, 2011). While the processes driving these transformations, such as thermal
63 disturbances, vegetation shifts, and subsidence, are relatively well-studied, their
64 consequences for GHG fluxes and C cycling remain uncertain, limiting our ability to project
65 future climate feedbacks (Holmes et al., 2022; Olefeldt et al., 2021; Turetsky et al., 2020).

66 Among the new landscape forms that emerge from degrading peat plateaus, thermokarst
67 ponds and wetlands play a critical role in greenhouse gas dynamics. These small aquatic
68 systems, formed by the thaw and collapse of permafrost, are characterized by high
69 concentrations of dissolved organic carbon (DOC) and inorganic carbon (DIC) (Abnizova et
70 al., 2012; Martin et al., 2021; Matveev et al., 2018). Thermokarst ponds, in particular, act as
71 hotspots for CH₄ and CO₂ emissions due to their unique biogeochemical conditions,
72 including hydrological isolation, anoxic sediments, and high organic matter availability (In 't
73 Zandt et al., 2020; Polishchuk et al., 2018; Vonk et al., 2015; Ward and Cory, 2015). Despite
74 their small size, these water bodies can contribute significantly to regional C fluxes, with CH₄
75 and CO₂ supersaturation levels often surpassing those of larger lakes or surrounding tundra
76 ecosystems (Abnizova et al., 2012; Kuhn et al., 2018; Shirokova et al., 2012). However, their
77 contributions are often overlooked in large-scale C assessments, as their small size makes
78 them difficult to detect using satellite-based methods (Holgerson and Raymond, 2016; Muster
79 et al., 2017).

80 As permafrost thaw progresses, the transition of isolated thermokarst ponds to interconnected
81 wetland systems further alters GHG dynamics. While northern permafrost wetlands currently
82 act as a C sink, the inclusion of thaw pond emissions into broader wetland carbon budgets
83 reveals their potential to offset the sink capacity by 39% (Kuhn et al., 2018). Compared to



84 thermokarst ponds, wetlands have sustained CH₄ fluxes over larger areas due to persistent
85 waterlogging and OM decomposition (Pirk et al., 2024; Swindles et al., 2015; Turetsky et al.,
86 2020), thus constituting important long term CH₄ sources (Bansal et al., 2023). The
87 transformation from stable permafrost to thermokarst landscapes is accompanied by shifts in
88 hydrology, OM lability, and microbial activity, which collectively shape CO₂ and CH₄
89 production pathways (Holmes et al., 2022; Laurion et al., 2020). Understanding the dynamics
90 of these evolving systems is critical for assessing the broader impacts of permafrost thaw on
91 regional C uptake and emissions as well as global C cycles.

92 Northern Norway's sporadic permafrost zone, with its abundant small thermokarst ponds and
93 emerging wetlands, provides a valuable opportunity to study these processes. The region's
94 rapidly degrading peat plateaus host significant C stocks, yet small aquatic systems,
95 especially those in Fennoscandia, remain underrepresented in Earth system models
96 (Abnizova et al., 2012; Muster et al., 2019; Muster et al., 2017). Existing studies emphasize
97 the importance of quantifying CH₄ and CO₂ fluxes in these environments and their
98 implications for C budgets (Abnizova et al., 2012; Matveev et al., 2018). However, critical
99 questions remain regarding how transitions between permafrost, thermokarst, and wetland
100 systems influence C dynamics, and whether these landscapes function as net C sources or
101 sinks under changing climatic conditions (Sim et al., 2021).

102 This study aims to address these gaps by examining the GHG dynamics and C
103 biogeochemistry of thermokarst ponds and wetland streams in the sporadic permafrost zone
104 of northern Norway. Over two years, we measured dissolved CO₂ and CH₄ concentrations,
105 water chemistry, and OM lability to evaluate the processes driving C fluxes in these systems.
106 We hypothesize that (1) thermokarst ponds serve as hotspots of CH₄ and CO₂ production
107 relative to wetland streams, (2) the transition from isolated ponds to wetlands significantly
108 alters GHG emission pathways, driven by shifts in hydrology and OC availability, and (3)



109 recently mobilized OM presents a labile source of C promoting CO₂ production in
110 thermokarst water bodies compared to wetland streams. By exploring these dynamics, this
111 study provides insights into the role of small water bodies in permafrost C feedbacks,
112 advancing our understanding of sub-Arctic and boreal C cycling.

113

114



115 2. Methods

116 2.1 Study area

117 The Iškoras field site (69.34°N, 25.29°E; 381 m a.s.l.) is a permafrost peatland plateau
118 located in the interior of the Finnmark province, northern Norway, on the Finnmarksvidda
119 plateau (Fig. 1). The region of Finnmarksvidda lies between 300 and 500 m a.s.l. and is
120 characterized by a subarctic continental climate. The topography was shaped by Pleistocene
121 glaciations, which deposited ground moraines, glaciofluvial, and glaciolacustrine sediments
122 (Sollid et al., 1973). The depressions in the landscape are commonly filled with peatlands
123 (Borge et al., 2017), and peat plateaus underlain by permafrost are common.

124 The Iškoras peat plateau covers an area of approximately 4 ha and is part of a 3.3 km²
125 subarctic headwater catchment that drains into the Báhkiljohka river (91 km²). Mean annual
126 air temperature and precipitation for the 30-year normal (1991-2020) period was $-1.9^{\circ}\text{C} \pm$
127 1.0°C , and 513 ± 90 mm, respectively (Table 1). For our study period 2021 to 2022, MAAT
128 and MAP were $-1.1^{\circ}\text{C} \pm 0.4^{\circ}\text{C}$, and 589.5 ± 62.5 (SeNorge, 2023). Iškoras lies within the
129 zone of sporadic permafrost and the peat soils extend down to about 1.5 m in the plateau
130 areas (Kjellman et al., 2018) and active layers depths up to 90 cm. The plateau exhibits a
131 complex surface of intact and degrading palsas, along with thermokarst ponds, and is
132 surrounded by wetlands and a stream to the northwest (Martin et al., 2019). Between 2019
133 and 2022, up to 0.8 m of subsidence of palsas was measured at localized sites (Pirk et al.,
134 2024). The site is located about 90 km south of the nearest coastal fjord and is dominated by
135 mountain birch forest (*Betula pubescens*) and tundra vegetation, including dwarf birch (*B.*
136 *nana*). The plateau consists primarily of low heath shrubs, Ericaceae (*Empetrum nigrum*,
137 *Rhododendron tomentosum*), lichen crusts, mosses, and cloudberry (*Rubus chamaemorus*) or
138 bare ground, while the surrounding wetlands are dominated by Sphagnum mosses, sedges
139 (*Carex* spp.), and cotton grass (*Eriophorum* spp.) (Kjellman et al., 2018; Martin et al., 2019).



	Unit	Mean ± std for 1991-2020	Mean + std for 2021-2022
annual temperature	°C	-1.9 ± 1.0	-1.1 ± 0.4
summer temperature	°C	10.4 ± 2.2	11.8 ± 0.2
annual precipitation	mm	513 ± 90	589.5 ± 62.5
summer precipitation	mm	196 ± 53	207 ± 48

140 **Table 1 Mean and standard deviation (std) of climate parameters for the Iškoras catchment for the**
141 **normal period (1991–2020) and the study period 2021–2022.** Summer is defined as May to
142 September.

143

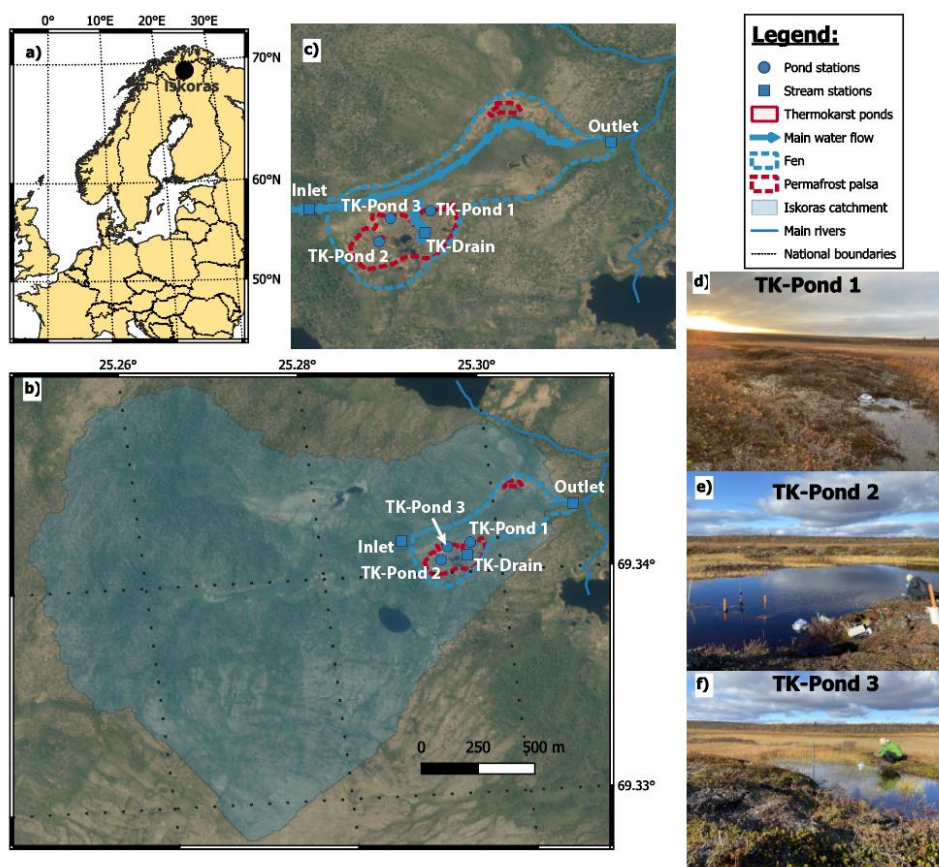
144 The study area included water bodies within a peat plateau and the adjacent wetland, selected
145 for sampling and monitoring. Measurements and samples were taken approximately monthly
146 in the ice-free season from May until October in 2021 and 2022. The waterbodies consisted
147 of three thermokarst ponds (TK-Pond 1, 2, and 3), a seasonal drainage channel (TK-Drain)
148 connecting the peat plateau to the wetland, and the wetland’s inlet and outlet streams (Inlet,
149 Outlet), with the outlet also marking the terminus of the Iškoras catchment. From mid-May to
150 early November, monitoring showed that the thermokarst ponds and Inlet were ice-free for
151 170 ± 5 days, while the Outlet remained ice-free for 184 days (Table SI 1).

152 The thermokarst ponds varied in hydrological connectivity and permafrost influence,
153 reflecting differences in age and physical characteristics. TK-Pond 1 (0.4 m depth) is small
154 and located at the peat plateau–wetland transition, experiencing periodic hydrological
155 isolation. TK-Pond 2, the largest and deepest (1.5 m depth), lies centrally on the peat plateau,
156 surrounded by degrading palsas. TK-Pond 3 (0.6 m depth) is situated at the plateau's edge and
157 was initially isolated by a surrounding permafrost mound.

158 The TK-Drain is a shallow, ephemeral drainage channel that provides the primary
159 hydrological connection between the peat plateau and wetland. The wetland’s inlet stream
160 (0.6 m wide, 15–40 cm deep) begins approximately 200 m upstream of the plateau, flowing
161 through birch forest and mires without permafrost before entering the wetland where the



162 channel becomes less defined. The outlet stream (0.8 m wide, 30–60 cm deep) re-emerges
163 approximately 700 m downstream at the wetland's far end, serving as the catchment outlet.
164 Between September 2020 and October 2022, a total of nine field campaigns were conducted
165 for regular sampling of water chemistry, dissolved gases, CO₂ emissions, dark incubations
166 and high-frequency monitoring of water height and temperature.



167
168 **Figure 1 Location map** of the study area in Europe (a) and the Iškoras catchment (b; determined
169 from the outlet station Outlet). Close-up of the wetland (c) with regular sampling sites and main
170 water flow direction. Pictures of the three main pond sites are also shown (d–f).



171 2.2 Water chemistry

172 Water samples for chemical analyses were collected using standardized procedures. From
173 each site, 500 mL unfiltered water was collected in HDPE rectangular bottles (Emballator
174 Melledrud AB, Stockholm, Sweden) after rinsing with sample waters three times, kept dark
175 after sampling, carried out of the field, and stored within hours after sampling at 4°C. The
176 samples were then transported by car and plane back to the laboratory and delivered for
177 chemical analysis where they were kept at 4°C until analysis. Chemical analysis of pH,
178 electrical conductivity (EC), alkalinity, sulfate (SO₄), silica (SiO₂), ammonium (NH₄), nitrate
179 (NO₃), total phosphorous (totP), total organic carbon (TOC), DOC (filtered by 0.45 µm) and
180 particulate organic carbon (POC) (filtered and then combusted at 1800 °C) in the water
181 samples was performed at accredited laboratories at the Norwegian Institute for Water
182 Research (NIVA); methods for analysis and quality control are described in Vogt and
183 Skancke (2022). The samples were not fully digested according to standard procedures
184 required for the determination of total nitrogen (totN), hence totN values are expected to be
185 underestimated and are therefore not shown in the manuscript (Thrane et al., 2020).

186 Absorption spectra of DOM were measured at NIVA for wavelengths between 200 and 900
187 nm, using 1 nm intervals, with a 5 cm cuvette length and Milli-Q water as a reference, using a
188 Lambda 40 UV/Vis spectrophotometer (Perkin Elmer, USA) and expressed in absorbance per
189 cm. In two samples, incomplete filtration caused excess scattering, and these spectra were
190 removed. The absorbencies were used to calculate specific UV absorbency (sUVa =
191 $A_{\lambda 254\text{nm}}/\text{mg C L}^{-1}$) and the specific UV absorption ratio (SAR = $A_{\lambda 254\text{nm}}/A_{\lambda 400\text{nm}}$).

192

193 2.3 Dissolved gas analysis

194 Dissolved gases (CO₂, CH₄) were sampled in the field using the acidified headspace
195 technique (Åberg and Wallin, 2014). Duplicate gas samples were collected according to



196 Valiente et al. (2022). Two 50 mL syringes were filled and sealed underwater without air
197 bubbles to prevent gas loss. Excess water was expelled to retain 30 mL, and 20 mL of
198 ambient air was drawn in to create a headspace. Samples were acidified with 0.6 mL of 3%
199 HCl to achieve $\text{pH} < 2$, ensuring DIC was present as CO_2 . Equilibrium was reached by
200 shaking for one minute, followed by a 30-second rest, repeated thrice. Fifteen mL of
201 headspace gas was transferred to 12 mL evacuated vials, and water temperature was
202 measured immediately after. Samples were stored at room temperature and flown to southern
203 Norway for analysis. A 15 mL ambient air sample was taken daily for background correction.
204 Analysis was performed via automated gas chromatography (GC) at the Norwegian
205 University of Life Sciences (NMBU), as described by Yang et al. (2015). A GC autosampler
206 (GC-Pal, CTC, Switzerland) injected 2 mL headspace samples into an Agilent 7890A GC
207 (Santa Clara, CA, USA) with a 20-m wide-bore Poraplot Q column at 38°C , using He as the
208 carrier gas to separate CH_4 and CO_2 from Ar, N_2 , and O_2 . For calibration, certified standards
209 of CO_2 and CH_4 in He were used (AGA, Germany) and N_2 , O_2 , and Ar were calibrated using
210 laboratory air. CH_4 was measured with a flame ionization detector (FID). A thermal
211 conductivity detector (TCD) was used to measure all other gases.

212 Dissolved gas concentrations were calculated from headspace concentrations corrected for
213 background air, applying temperature-adjusted Henry's law constants (Wilhelm et al., 1977)
214 based on the recorded water temperature. At $\text{pH} > 4$, a non-negligible amount of DIC is in the
215 form of (bi)carbonates (HCO_3^- , CO_3^{2-}). The bicarbonate concentrations were calculated based
216 on pH , dissolved CO_2 and the temperature-adjusted first dissociation constant ($\text{pK}_1 = 6.41$ at
217 25°C ; Stumm and Morgan (2013)) of the carbonic acid equilibrium. Dissolved CO_2 was
218 calculated as DIC minus bicarbonate. To facilitate comparisons with existing studies that
219 report dissolved gases in μatm , we converted dissolved gas concentrations to CO_2 or CH_4



220 saturation indexes (GHG_{SI}) assuming atmospheric partial pressures of CO₂ and CH₄ as 400

221 μatm and 1.9 μatm , respectively:

$$222 \quad GHG_{SI} = \frac{[GHG]}{[GHG]_{saturation}}$$

223 Where $[GHG]$ is the measured dissolved CO₂ or CH₄ concentration, and $[GHG]_{saturation}$ is

224 the concentration of dissolved CO₂ or CH₄ at equilibrium with their respective atmospheric

225 partial pressure.

226

227 2.4 Diffusive CO₂ fluxes from water to atmosphere

228 Measurements of CO₂ fluxes from water to atmosphere (diffusive CO₂ fluxes) were measured

229 at each site for 30-60 minutes using self-made, opaque flux chambers as described by

230 Bastviken et al. (2015) at the water-air interface. The chamber consists of a Senseair K30

231 sensor (Senseair AB, Delsbo, Sweden) housed within a plastic bucket that records pCO₂,

232 temperature, and relative humidity every 30 seconds. Fluxes are calculated from the linear

233 increase in pCO₂ corrected for ambient temperature and humidity in the chamber (Bastviken

234 et al., 2015) considering the internal air volume and the water surface area covered by the

235 chamber. Single measurements with a linear increase in pCO₂ with time associated with a

236 coefficient of determination (R^2) lower than 0.9 were discarded.

237

238 2.5 Dark incubations

239 Water samples were collected for short term dark incubations started directly in the field

240 lasting between 18 and 30 hours to estimate DOM mineralization and GHG processing rates.

241 Serum flasks (120 mL) were filled with 80 mL of water with a 50 mL syringe equipped with

242 a long tube. The syringe was filled and closed under water, and the water was gently pushed

243 at the bottom of the serum flask to prevent gas loss. The remaining 40 mL were left with

244 ambient air as headspace. The flasks were crimp-sealed with gas-tight, butyl-rubber septa,



245 sealed, covered with aluminium foil and kept at field temperature (for maximum 6 hours),
246 transported back from the field to be stored at room temperature (18-20°C). The day
247 following the sampling (18 to 30 hours after sampling), the incubations were stopped by
248 adding 1.6 mL 3% HCl to reach a final pH below 2, after which gas samples were taken
249 following the protocols described above. Results from the dark incubation were expressed as
250 rates of DIC production over the course of the incubation period by comparison with initial
251 DIC concentrations and reported as μMh^{-1} :

$$252 \quad DIC_{rate} = \frac{[DIC]_f - [DIC]_0}{h} \quad (\text{Eq. 2})$$

253 where $[DIC]_f$ is the final solute concentrations in the dark incubation and $[DIC]_0$ is the initial
254 solute concentration taken in the field (see Sect 2.3) in μM , and h is the incubation duration
255 in hours. In addition, we normalized the DIC production rate with DOC concentration to
256 estimate DOM mineralization rates (per time unit). Also, we calculated the first-order DOM
257 decay rate (yr^{-1}) using the exponential decay rate model (Mostovaya et al., 2017). The
258 exponential decay model, based on early studies on sediment diagenesis (Boudreau and
259 Ruddick, 1991; Westrich and Berner, 1984), is often the best model to describe decay rates
260 from bioassays in closed systems (Vähätalo et al., 2010) and has been widely used to describe
261 DOM degradation reactions. Under the exponential decay model, the decay constant (k_{DOM} ;
262 yr^{-1}) can be expressed as:

$$263 \quad k_{DOM} = \ln \left(\frac{DOC}{DOC - ([DIC]_f - [DIC]_0) M_C} \right) \times \frac{8766}{h} \quad (\text{Eq. 3})$$

264 where DOC is the DOC concentration in $\mu\text{g L}^{-1}$, M_C is the molecular mass of C in g mol^{-1} and
265 8766 is the number of hours in a year. Where $[DIC]_f$ was equal to or below $[DIC]_0$, we
266 removed the values from the dataset assuming that the temperature correction of $[DIC]_0$ was
267 not precise enough (three of 39 samples) to allow quantification of CO_2 processing rates.



268 These occurred in September 2020 and October 2021, under cold field conditions, when

269 $[DIC]_0$ was overestimated because of unknown sample temperature in the field.

270

271 2.6 Statistical methods

272 Statistical analyses were conducted to evaluate differences between sites for various

273 measured parameters. One-way analysis of variance (ANOVA) was employed to test for

274 differences among groups. Pairwise comparisons of group means were performed using

275 Student's t-test using JMP 18.0.11 (2024 JMP Statistical Discovery LLC). For data that did

276 not conform to normal distribution assumptions, non-parametric methods were applied,

277 specifically the Wilcoxon rank-sum test, to ensure robust comparisons across sites. Results

278 are displayed in the form of connecting letters reports within the tables. Sites with the same

279 letter (e.g., "A" or "B") indicate no statistically significant differences in the measured

280 parameter between those groups at the $p < 0.05$ significance level. Groups with different

281 letters (e.g., "A" vs. "B") are significantly different. When overlapping letters (e.g., "AB") are

282 reported, those groups are statistically similar to others with at least one shared letter but may

283 differ from groups with entirely distinct letters. Figures were created using the ggplot2

284 package (Wickham, 2016) using R software (R Core Team, 2021).



285 3. Results

286 3.1 Water chemistry

287 The thermokarst water bodies were more acidic, richer in DOC and total P, and lower in SO₄
288 and SiO₂ compared with the wetland streams (all differences statistically significant; Table 2;
289 Fig. 2). The low pH of the ponds is consistent with their high DOC, and thus high organic
290 acidity. The water bodies aligned along the inverse DOC-pH relationship with TK-Pond 3 at
291 the top, followed by TK-Pond 2 and TK-Pond 1. The TK-Drain usually held an intermediate
292 position between the thermokarst ponds and the wetland streams, which were found at the
293 high pH – low DOC end of the curve. Similar patterns were found for DOC-SO₄ and DOC-
294 SiO₂ relationships (Fig. 2). Particulate OC was on average <5% of TOC in the wetland
295 streams, while POC showed considerably more variation in the thermokarst water bodies,
296 possibly related to inputs from destabilized organic matter from the thawing permafrost.
297 All water bodies had NO₃ concentrations at, or close to, the detection limit, while the
298 thermokarst water bodies had considerable levels of NH₄ contrary to the wetland streams
299 (Table 2). Despite incomplete digestion prior to totN determination, totN values were enough
300 to confirm that the dominant form of N was organic. Total P was highest, and most variable,
301 in the ponds which to some extent mirrored the pattern in DOC, understandably given that in
302 these nutrient-poor sites most P would be in an organic form just like N.

303 The DOM quality indicator SAR was highest in the thermokarst ponds ($p < 0.03$). SAR was
304 positively strongly correlated with DOC concentration (positive, R^2 0.57, $p < 0.0001$),
305 implying that lowest SAR was found in the wetland streams. Other DOM quality indicators
306 (sUV_a, associated with aromaticity) tended to be somewhat higher in the wetland streams but
307 did not show significant differences between wetlands and thermokarst water bodies.

308



309 **Table 2. Water chemistry parameters for thermokarst ponds and wetland sites during nine**
 310 **sampling campaign.** Median values with standard deviations are shown for all water chemistry
 311 variables, except for pH, which is shown as the median with minimum and maximum values. EC:
 312 electrical conductivity; SO₄: Sulfate; SiO₂: silica; DOC: dissolved organic carbon; sUVa: specific UV
 313 absorbency, SAR: specific UV absorption ratio; TOC: total organic carbon; NH₄: ammonium; NO₃:
 314 nitrate, totP: total organic phosphorous; POC: particulate organic carbon (POC, % of TOC). Letters
 315 indicate significant differences between sites for each variable (Tukey's *t*-test, pairwise comparisons,
 316 *p*<0.05; see Sect. 2.6).

	pH		EC mS m ⁻¹		SO ₄ mg SO ₄ L ⁻¹		SiO ₂ mg SiO ₂ L ⁻¹	
TK-Pond 1	4.49 (4.16-4.79)	B	2.1 (0.7)	B	0.12 (0.07)	C	2.4 (1.8)	BC
TK-Pond 2	4.23 (4.03-4.37)	C	3.2 (0.7)	A	0.18 (0.20)	C	1.0 (1.0)	C
TK-Pond 3	4.06 (3.79-4.32)	C	4.0 (1.6)	A	0.11 (0.02)	C	4.3 (1.7)	B
TK-Drain	4.79 (4.63-4.88)	B	1.6 (0.1)	B	0.16 (0.08)	C	2.3 (1.9)	BC
Inlet	6.69 (6.11-7.36)	A	2.0 (0.5)	B	0.85 (0.18)	A	8.7 (2.4)	A
Outlet	6.56 (6.04-6.97)	A	1.9 (0.3)	B	0.60 (0.25)	B	8.6 (3.0)	A

	DOC mg C L ⁻¹		sUVa A _{λ254nm} /mg C L ⁻¹		SAR A _{λ254nm} /A _{λ400nm}		TOC mg C L ⁻¹	
TK-Pond 1	19.2 (4.4)	C	3.9 (0.4)	ABC	8.4 (0.3)	BC	20.8 (5.1)	C
TK-Pond 2	25.7 (6.4)	B	4.2 (0.3)	A	8.8 (0.5)	AB	27.4 (7.7)	B
TK-Pond 3	34.1 (6.8)	A	3.6 (0.6)	BC	9.2 (0.7)	A	34.8 (9.4)	A
TK-Drain	17.3 (6.6)	C	3.8 (0.4)	C	8.1 (0.2)	AB	19.5 (4.5)	C
Inlet	8.5 (2.1)	D	4.1 (0.4)	AB	7.6 (0.2)	C	8.4 (1.6)	D
Outlet	9.0 (1.5)	D	4.3 (0.3)	A	7.8 (0.2)	C	9.4 (1.6)	D

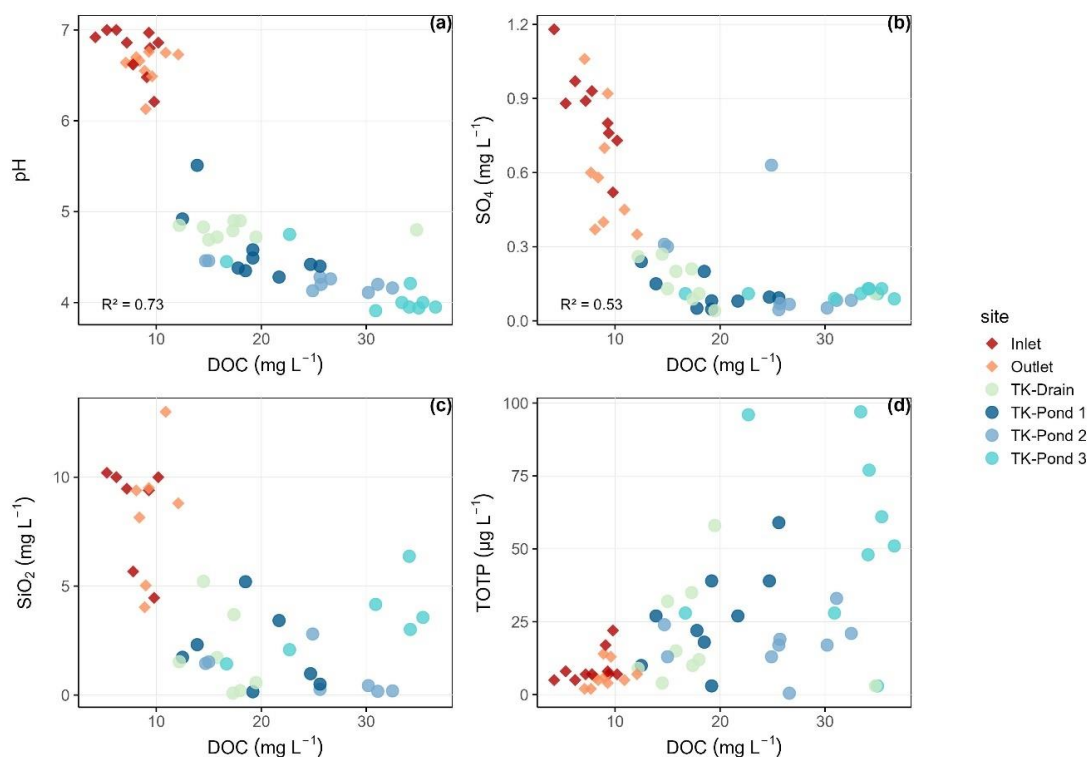
	NH ₄ μg N L ⁻¹		NO ₄ μg N L ⁻¹		TotP μg P L ⁻¹		POC % of TOC	
TK-Pond 1	23 (26)	B	2.0 (0.0)	A	27 (17)	B	5.6 (3.0)	B
TK-Pond 2	94 (105)	A	2.1 (0.3)	A	18 (9)	BC	6.1 (4.1)	B
TK-Pond 3	38 (77)	AB	1.9 (0.3)	A	54 (32)	A	8.2 (5.9)	B
TK-Drain	33 (20)	B	2.0 (0.0)	A	20 (18)	BC	17.1 (11.6)	A
Inlet	2 (2)	B	1.9 (0.3)	A	9 (6)	C	4.4 (1.8)	B
Outlet	4 (8)	B	1.9 (0.3)	A	7 (4)	C	4.1 (1.9)	B

317



318 The inverse relationship between DOC and pH points towards organic acidity as a strong
319 driver of pH. Additionally, the near-to-neutral pH in the wetland streams is consistent with
320 groundwater influences from the catchment, which also would explain the elevated SiO₂ and
321 SO₄ concentrations. A limited set of water samples were analysed for base cations (Table SI
322 3), confirming that these were highest in the wetland streams.

323 The water chemical composition of the ponds mirrored the impact of thawing permafrost: the
324 TK-Pond 3 is hydrologically most isolated with the lowest pH, highest conductivity, and
325 highest DOC. TK-Pond 1, located at the transition from peat plateau to wetland, had a higher
326 pH and lower EC, DOC and NH₄ than the other ponds, which is consistent with some
327 hydrological influences from the wetland and hence less permafrost impact. TK-Pond 2 is
328 located in the middle of the peat plateau and is by far the largest pond and, under wet
329 conditions, hydrologically connected to neighbouring ponds. The water chemistry of TK-
330 Drain was usually most similar to that of TK-Pond 1. An example of pH and EC gradients
331 from the peat plateau into the wetland is consistent with the influence of thermokarst
332 waterbodies gradually becoming less dominant in the transition from the peat plateau
333 complex to the wetland (Fig. S11).



334

335 **Figure 2. Relationships between Dissolved Organic Carbon (DOC) and various water quality**

336 **parameters across different sites.** The scatter plots demonstrate the relationships between

337 dissolved organic carbon (DOC) and pH (a), sulfate (SO₄) (b), silica (SiO₂) (c), and total organic

338 phosphorus (totP) (d).

339

340 3.2 Dissolved gases and gas evasion

341 All water bodies were oxygenated and dissolved O₂ concentrations were on average 61 to

342 81% of water O₂ saturation (Table 3). The ponds are shallow which allow for wind mixing

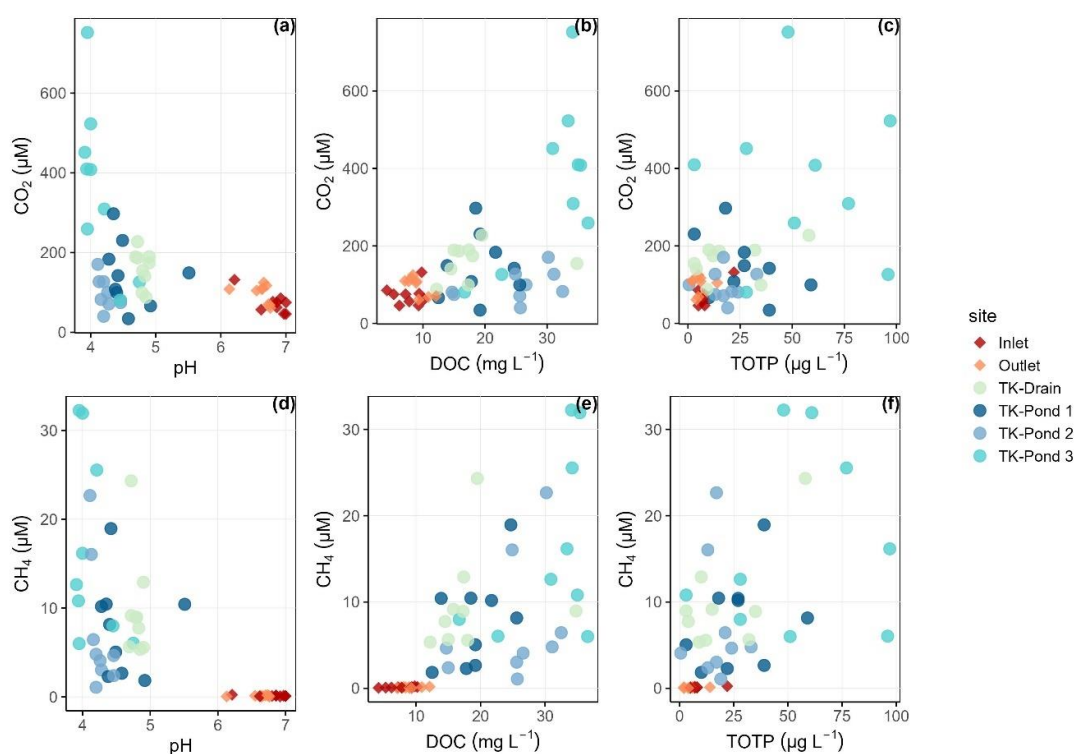
343 and they host sphagnum, suggesting active O₂ production through photosynthesis. All water

344 bodies were oversaturated with CH₄ and CO₂. Dissolved CH₄ concentrations were 2000–5000

345 and ~30 times higher than atmospheric equilibrium, in the ponds and in the wetland streams,



346 respectively, indicating that all water bodies – thermokarst ponds in particular - are net
347 sources of CH₄ to the atmosphere. The lower CH₄ oversaturation in streams compared with
348 ponds is likely related to higher CH₄ losses caused by stream turbulence and/or higher
349 production rates of CH₄ in the thermokarst ponds (Fig. 3).

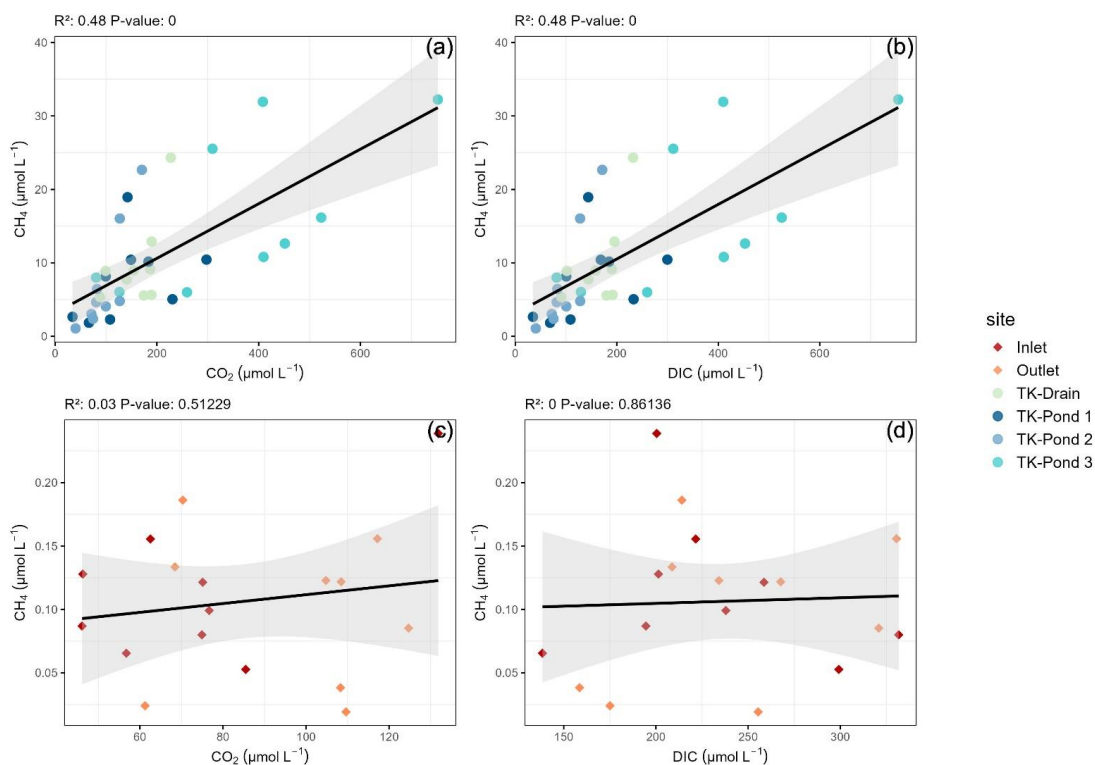


350

351 **Figure 3 Variations in carbon dioxide (CO₂) and methane (CH₄) concentrations in relation to pH,**
352 **DOC, and totP across sampling sites.** The upper panels show the relationships between CO₂
353 concentrations (μM) and pH (a), dissolved organic carbon (DOC, mg L⁻¹) (b), and total organic
354 phosphorous (totP, μg L⁻¹) (c).
355 CO₂ saturation indexes in the thermokarst waterbodies reached 5 to 20 while in the streams
356 they ranged between 3 and 4. By contrast, the CO₂ evasion from the streams (e.g. 1-2 g C m⁻²
357 day⁻¹) was higher than from the ponds (0.3-0.5 C m⁻² day⁻¹), consistent with the higher
358 turbulence in the streams, and the replenishment of CO₂ from bicarbonates from groundwater



359 in these streams, which is a geological rather than a recent source of CO₂. Bicarbonates
360 contributed about 60-70% to DIC in the wetland streams (with pH between 6.0 and 7.4),
361 while bicarbonates in thermokarst water bodies were almost negligible (with pH below 4.5),
362 which is consistent with equilibrium between bicarbonates and CO₂ over these pH ranges.
363 TK-pond 3 had the lowest O₂ concentrations and the highest CH₄ and CO₂ concentrations of
364 all thermokarst water bodies. Concentrations of CH₄ and DIC were positively related in the
365 thermokarst water bodies (r^2 0.48, $p < 0.0001$, F-test) but not in the wetland streams (Fig. 4).



366

367 **Figure 4** Relationships between CH₄ and (a) CO₂, (b) DIC for thermokarst waterbodies, and (c) CO₂,
368 (d) DIC for Inlet and Outlet sites including linear regression lines and corresponding R² and p-value
369 statistics. Note scale differences for CH₄ between thermokarst waterbodies and the wetland
370 streams.



371 The CO₂ emissions from the stream sites (Inlet and Outlet) were substantially larger than
 372 those from the thermokarst waterbodies (Table 3). The mean CO₂ emission at the Inlet site
 373 was $1.12 \pm 0.46 \text{ g C m}^{-2} \text{ day}^{-1}$, and at the Outlet site $2.20 \pm 1.15 \text{ g C m}^{-2} \text{ day}^{-1}$. These values
 374 are 3 to 7 times higher than the fluxes observed from the thermokarst waterbodies, which
 375 ranged from $0.30 \pm 0.22 \text{ g C m}^{-2} \text{ day}^{-1}$ (TK-Pond 2) to $0.51 \pm 0.28 \text{ g C m}^{-2} \text{ day}^{-1}$ (TK-Pond 3).

376 Annual CO₂ fluxes for the ice-free period, assuming negligible flux during the ice-covered
 377 months, ranged between $51 \text{ g C m}^{-2} \text{ yr}^{-1}$ and $87 \text{ g C m}^{-2} \text{ yr}^{-1}$ for the thermokarst ponds, and
 378 the streams ranged between $190 \text{ g C m}^{-2} \text{ yr}^{-1}$ (Inlet) and $405 \text{ g C m}^{-2} \text{ yr}^{-1}$ (Outlet).

379 **Table 3. Mean and standard deviations of dissolved gas concentrations and associated metrics for**
 380 **thermokarst ponds and wetland sites across nine sampling campaigns.** Mean concentrations of CO₂
 381 (μM) and CH₄ (μM) with their respective saturation ratios, along with CO₂ emission flux (g C m⁻² day⁻¹)
 382 ¹), DIC (μM), and oxygen concentrations (μM) with percent saturation. The saturation ratio is defined
 383 as the concentration divided by the equilibrium concentration between the atmosphere and water
 384 at the given temperature. For this study, DIC is considered the sum of dissolved CO₂ and
 385 bicarbonate. Letters indicate significant differences between sites for each variable.

	CO ₂		DIC	CO ₂ emission
	μmol L ⁻¹	Saturation ratio CO ₂	μmol L ⁻¹	g C m ⁻² day ⁻¹
TK-Pond 1	146 (82) B	7.0 (3.2) BC	149 (83) BC	0.36 (0.28) C
TK-Pond 2	97 (39) B	5.1 (2.2) BC	98 (39) C	0.30 (0.22) C
TK-Pond 3	369 (206) A	18.8 (11.3) A	371 (206) A	0.51 (0.28) C
TK-Drain	161 (45) B	8.1 (2.7) B	165 (46) BC	0.37 (0.15) C
Inlet	73 (26) B	3.1 (1.0) C	232 (59) B	1.12 (0.46) B
Outlet	97 (24) B	4.4 (1.1) BC	241 (59) B	2.20 (1.15) A

	CH ₄	CH ₄ saturation ratio	O ₂	% saturation
	μmol L ⁻¹		μmol L ⁻¹	
TK-Pond 1	7.8 (5.5) B	2 330 (1 719) B	273 (59) AB	81 (14) A
TK-Pond 2	7.2 (7.2) B	2150 (2 110) B	266 (85) AB	79 (19) A
TK-Pond 3	16.6 (10.6) A	5 109 (3 470) A	210 (89) B	61 (22) B
TK-Drain	9.8 (5.9) B	2976 (1973) B	260 (65) AB	77 (18) AB
Inlet	0.1 (0.1) C	30 (15) C	297 (59) A	81 (14) A



386 Outlet 0.1 (0.1) C 28 (18) C 241 (63) AB 67 (14) AB

387 3.3 DOM processing rates

388 Average DIC production rates in the different water bodies were highly variable (5.8 – 35.7
 389 $\mu\text{M day}^{-1}$, Table 4), but tended to be highest in the thermokarst ponds compared with the
 390 wetland streams, while the TK-drain had the lowest rates (Tukey’s t-test, $p < 0.05$. The non-
 391 parametric Wilcoxon tests supported these trends, confirming minimal site-specific effects
 392 overall, with TK-Drain showing lower activity). These results reflect the in-situ processing of
 393 DOM in both thermokarst ponds and streams. The DOM mineralization rate did not vary
 394 significantly between sites and neither did the exponential decay rate $k\text{DOM}$ (Table 4).
 395 $k\text{DOM}$ in the thermokarst ponds ranged from 5.5 yr^{-1} to 6.7 yr^{-1} (Table 4), while the stream
 396 showed higher $k\text{DOM}$ values from 8.3 yr^{-1} to 8.8 yr^{-1} . The TK-Drain site was substantially
 397 lower (2.0 yr^{-1}).

398 **Table 4. Rates of production and decay.** DIC rates reflect DIC production. The DIC rate/DOC ratio
 399 indicates the relative efficiency of converting DOC to DIC, while $k\text{DOM}$ indicates the exponential
 400 decay rate of DOM, showing how quickly DOM is decomposed over time. Letters indicate significant
 401 differences between sites for each variable ($p < 0.05$).

	DIC rate $\mu\text{mol day}^{-1}$		DIC rate/DOC $\mu\text{mol g C}^{-1} \text{day}^{-1}$		$k\text{DOM}$ yr^{-1}	
TK-Pond 1	26.7 (13.7)	AB	62.9 (34.2)	A	6.7 (3.7)	A
TK-Pond 2	34.5 (39.5)	B	62.3 (74.3)	A	6.7 (8.2)	A
TK-Pond 3	35.7 (33.9)	A	51.2 (36.3)	A	5.5 (4.0)	A
TK-Drain	5.8 (6.1)	B	19.2 (21.2)	A	2.0 (2.3)	A
Inlet	18.8 (11.3)	B	77.3 (27.5)	A	8.3 (3.0)	A
Outlet	20.5 (16.7)	AB	82.0 (64.7)	A	8.8 (7.0)	A

402 4. Discussion

403 4.1 Thermokarst ponds as hotspots of methane emissions

404 Thermokarst ponds in Iškoras display CH_4 saturation indexes of 2300 to 5000, which is
 405 among the highest values reported in the literature for natural waterbodies. These findings



406 align with Shirokova et al. (2012) and Matveev et al. (2018) who documented saturation
407 indexes of 50 to 5000 in Siberian thermokarst depressions, and of 5 to 50 in subarctic lithalsa
408 lakes, respectively. Such high CH₄ concentrations in these poorly connected, small, and
409 relatively protected water bodies are consistent with the established inverse relationship
410 between CH₄ concentrations and water body size, hydrological connectivity, and turbulence
411 exposure (Abnizova et al., 2012; Kankaala et al., 2013; Polishchuk et al., 2018). Similarly, at
412 Iškoras, the smallest pond exhibited the highest CH₄ oversaturation, in combination with the
413 highest DOC, totP, and lowest pH values, likely linked to destabilization of thawing
414 permafrost combined with limited hydrological connectivity. In fact, low pH and elevated
415 totP concentrations are commonly related to increased DOM concentrations (Holmes et al.,
416 2022; Ward and Cory, 2015), which could originate from destabilized permafrost (Turetsky
417 et al., 2020).

418 Thermokarst ponds were highly oversaturated in CH₄ despite the presence of dissolved O₂.
419 CH₄ production is known to occur mainly in anoxic sediments (Bastviken et al., 2004; Clayer
420 et al., 2016; Wik et al., 2016), from where CH₄ is subsequently transported to overlying
421 water. The microbial activity responsible for CH₄ production may be enhanced by fresh OM
422 input from ongoing thermokarst development (Crevecoeur et al., 2017), as recently observed
423 in laboratory incubations with recently inundated peat material from the Iškoras site (Kjær,
424 2024).

425 4.2 Impact of thawing peat plateaus on water chemistry

426 The transition of permafrost-underlain peat plateaus to thermokarst ponds and further to
427 wetlands can markedly shift the landscape-scale GHG dynamics as permafrost continues to
428 thaw (Hugelius et al., 2020; Sannel and Kuhry, 2011). Thermokarst ponds are localized CH₄
429 hotspots; however, as these systems transition into wetlands, emissions patterns change due
430 to altered hydrology and biogeochemistry (Holmes et al., 2022; Peura et al., 2019). In



431 wetlands, persistent inundation creates anoxic conditions favourable for methanogenesis,
432 often leading to significant CH₄ emissions (Cui et al., 2024). Pirk et al. (2024) demonstrated
433 that fens at Iškoras, as an example of such inundated wetland systems, emit large amounts of
434 CH₄, particularly where fresh organic carbon is available from peat decomposition from
435 degrading palsa edges. Similarly, Turetsky et al. (2020) noted that newly formed wetlands,
436 arising from permafrost thaw become additional CH₄ sources due to labile OC availability.

437 Holmes et al. (2022) observed that inundation in permafrost landscapes increases CH₄
438 emissions because of waterlogged conditions that limit oxygen diffusion and enhance
439 anaerobic decomposition. Additionally, Kjær et al. (2024) highlighted that recently thawed
440 permafrost peat in wetland systems, including peat from Iškoras, features a high CH₄
441 production potential due to the presence of labile C and methanogenic microbial
442 communities.

443 Unlike thermokarst ponds, which are spatially limited, wetlands have a wider spatial extent.
444 The carbon balance in wetlands depends not only on CH₄ fluxes but also on changes in CO₂
445 dynamics as organic matter mineralization occurs under waterlogged conditions (Turetsky et
446 al., 2020). In this context, the transition from thermokarst ponds to wetlands represents a shift
447 from localized emissions of both CH₄ and CO₂ emissions to more spatially homogenous CH₄
448 emissions, while CO₂ is sequestered (Pirk et al., 2024).

449 Although a focus on vertical fluxes dominates many studies, lateral DOC fluxes also play a
450 role in carbon dynamics in permafrost-affected systems. Wetland and peatland ecosystems
451 exhibit high rates of lateral DOC export due to hydrological connectivity (Tank et al., 2018).
452 Beckebanze et al. (2022) reported that lateral fluxes, though smaller in magnitude compared
453 to vertical fluxes, are essential in carbon budgets, potentially contributing to carbon loss
454 especially during peak runoff events. These lateral DOC fluxes transport carbon from soils to



455 aquatic systems, where it may later contribute to downstream GHG emissions or C
456 sequestration. The potential for fens and wetlands to transition into significant GHG
457 contributors and increased hydrological connectivity leading to greater potential lateral C
458 fluxes highlights the need for integrated C budget models that capture the evolving landscape
459 dynamics in permafrost regions.

460 4.3 Carbon dioxide dynamics in thermokarst water bodies
461 Both thermokarst ponds and streams in Iškoras are oversaturated with CO₂, a common feature
462 of Arctic and subarctic aquatic systems (Alleson et al., 2022; Bastviken et al., 2004).
463 However, the mechanisms driving CO₂ fluxes differ between ponds and streams. In ponds,
464 despite high CO₂ concentrations, CO₂ release is lower than in streams and likely limited by
465 the lack of turbulence. By contrast, streams exhibit enhanced CO₂ fluxes due to high
466 turbulence and carbonate inputs, as described by Zolkos et al. (2019), who emphasized the
467 role of groundwater-derived bicarbonates in sustaining CO₂ fluxes in Arctic streams.

468 Quantitatively, CO₂ efflux from streams at Iškoras averages 0.4 g C m⁻² day⁻¹, aligning
469 closely with values observed in Siberian permafrost streams (0.3–0.5 g C m⁻² day⁻¹;
470 (Shirokova et al., 2012)). This flux reflects the significant contribution of turbulent flow and
471 bicarbonate-rich groundwater inputs, processes shown to facilitate CO₂ release (Lundin et al.,
472 2013; Raymond et al., 2013). Streams benefit from continuous replenishment of CO₂ from
473 bicarbonates, which account for 60–70% of DIC in these environments (Wallin et al., 2018;
474 Zolkos and Tank, 2020).

475 In contrast, CO₂ emissions from ponds at Iškoras are notably lower, similar to findings of
476 Campeau and Del Giorgio (2014), attributed to the ponds' high DOC-to-bicarbonate ratios,
477 which restrict bicarbonate formation and subsequent CO₂ production (Abnizova et al., 2012;
478 Bastviken et al., 2004). The limited water mixing in ponds further diminishes CO₂ flux due to
479 low gas exchange rates compared to streams. However, DIC production rates in ponds (26.7–



480 35.7 $\mu\text{M day}^{-1}$) remain sufficient to sustain CO_2 effluxes of 5–10 $\text{mol C m}^{-2} \text{ year}^{-1}$, consistent
481 with findings by (Shirokova et al., 2012), who linked DIC production directly to DOC
482 concentrations in Arctic aquatic systems. These DIC production rates are relatively high
483 compared to other reported values in the literature (Catalán et al., 2016).

484 High CO_2 evasion from lower-order streams is caused by high flow velocities and associated
485 turbulence causing high gas exchanges (Schelker et al., 2016). These drivers likely explain
486 the relatively higher CO_2 efflux from Iškoras streams compared to ponds. Furthermore, DOM
487 lability, influenced by pH and nutrients, plays a critical role. High molecular-weight DOM, as
488 indicated by low SUVA and SAR values, can inhibit microbial oxidation, thereby slowing
489 DOM decay rates (Shirokova et al., 2019). Ward and Cory (2015) also noted that DOM from
490 thawing permafrost, while less aromatic and more labile compared to active layer DOM, may
491 become limited by environmental factors such as pH and nutrient availability, resulting in
492 lower mineralization rates. The acidic conditions in ponds could shift microbial communities
493 and affect activity (Vigneron et al., 2019), a factor that can further limit CO_2 fluxes from
494 ponds in addition to the low gas exchange rate.

495 In summary, the higher CO_2 fluxes observed in streams at Iškoras are likely driven by the
496 combined effects of turbulent flow, bicarbonate input, and mineral weathering, whereas lower
497 emissions from ponds are shaped by organic acidity, limited hydrological connectivity, and
498 lack of turbulence. These dynamics emphasize the need to account for the interplay of
499 hydrological and chemical factors when assessing C fluxes in permafrost-impacted regions.

500 4.4 Climate feedback implications

501 The distinct roles of CH_4 and CO_2 in the Iškoras landscape underscore their unique climate
502 feedback potentials. The transition from thermokarst ponds to wetlands modifies the overall
503 GHG footprint of the peatland-wetland continuum, balancing the loss of localized CH_4
504 emission hotspots with the emergence of sustained, long-term CH_4 emissions from wetlands,



505 while the fate of organic matter currently stored in permafrost remains uncertain. At the same
506 time, CO₂ fluxes from the streams and rivers may increase due to enhanced hydrological
507 connectivity and increased organic matter input (Zolkos et al., 2019), in agreement with the
508 results of our study. These findings reflect the complex interplay of ecological and
509 hydrological factors shaping GHG emissions in permafrost landscapes. Turetsky et al. (2020)
510 and Pirk et al. (2024) both emphasized the need for further research on spatiotemporal
511 variability, particularly during thaw cycles, to refine predictions of permafrost C feedbacks.

512

513 5. Conclusions

514 This study highlights the distinct biogeochemical roles of thermokarst ponds and wetland
515 streams in a landscape of sporadic permafrost in subarctic Norway. Thermokarst ponds at the
516 Iškoras site, characterized by low pH, high organic acidity, and elevated DOC concentrations,
517 are currently hotspots for CH₄ emissions, with stable DOM lability driving sustained carbon
518 processing. In contrast, wetland streams exhibit higher CO₂ fluxes, largely driven by
519 turbulence and bicarbonate replenishment from groundwater. Despite similarities in DOM
520 mineralization rates between ponds and streams, environmental constraints, such as pH,
521 microbial community composition, and hydrodynamic mixing, are likely controls of the
522 observed differences in GHG fluxes. As thermokarst ponds transition into wetlands, they will
523 no longer function as hotspots for CH₄ emissions. Instead, CH₄ emissions are likely to
524 increase across the entire landscape, as sustained waterlogging promotes elevated CH₄
525 production. These ecological shifts, coupled with lateral DOC losses from peat plateaus,
526 highlight the importance of hydrological connectivity in linking terrestrial and aquatic C
527 dynamics. Such transitions emphasize the need for integrated C budget models that account
528 for the evolving contributions of small aquatic systems to regional and global C cycles.



529 Future research should prioritize direct measurements of CH₄ fluxes, microbial community
530 contributions to DOM decomposition under varying environmental constraints, and the
531 temporal variability of gas production and emissions. Additionally, exploring seasonal
532 dynamics, lateral carbon transport, and hydrological processes will provide critical insights
533 into C cycling. Investigating catchment-scale signals, such as DOC concentrations across
534 entire river systems and their links to permafrost contributions, can further advance our
535 understanding of landscape-level processes. By addressing these questions, we can better
536 predict the trajectory of permafrost-impacted landscapes and their feedbacks to the global C
537 cycle in a warming climate.

538 Data availability

539 All data supporting this study will be made available on a permanent repository upon
540 acceptance.

541 Author contributions

542 JKK and HDW conceptualized the study. JKK, HDW and FC participated in data collection.
543 JKK, FC, HDW and PD conducted the experiments and performed data analysis. JKK, HDW
544 and FC created the figures. JKK and HDW drafted the initial manuscript, and HDW, FC, SW
545 and PD revised and edited the final version.

546 Competing interests

547 The authors declare that they have no conflict of interest.

548 Acknowledgements



549 NIVA core funding (Research Council of Norway, contract nr 342628/L10) Global Change at
550 Northern Latitudes, BIOGOV project (Research Council of Norway, project nr 323945), Uta
551 Brandt, Hanna Lee, Inge Althuizen, Emelie Forsman
552



553 References

- 554 Abnizova, A., Siemens, J., Langer, M., and Boike, J.: Small ponds with major impact: The relevance of
555 ponds and lakes in permafrost landscapes to carbon dioxide emissions, *Global*
556 *Biogeochemical Cycles*, 26, 2, <https://doi.org/10.1029/2011GB004237>, 2012.
- 557 Alewell, C., Giesler, R., Klaminder, J., Leifeld, J., and Rollog, M.: Stable carbon isotopes as indicators
558 for environmental change in peatlands, *Biogeosciences*, 8, 1769–1778,
559 <https://doi.org/10.5194/bg-8-1769-2011>, 2011.
- 560 Allesson, L., Valiente, N., Dorsch, P., Andersen, T., Eiler, A., and Hessen, D.O.: Drivers and variability
561 of CO₂:O₂ saturation along a gradient from boreal to Arctic lakes, *Sci. Rep.*, 12, 18989,
562 <https://doi.org/10.1038/s41598-022-23705-9>, 2022.
- 563 Bansal, S., Post van der Burg, M., Fern, R.R., Jones, J.W., Lo, R., McKenna, O.P., Tangen, B.A., Zhang,
564 Z., and Gleason, R.A.: Large increases in methane emissions expected from North America's
565 largest wetland complex, *Sci. Adv.*, 9, eade1112, <https://doi.org/10.1126/sciadv.ade1112>,
566 2023.
- 567 Bastviken, D., Cole, J., Pace, M., and Tranvik, L.: Methane emissions from lakes: Dependence of lake
568 characteristics, two regional assessments, and a global estimate, *Global Biogeochemical*
569 *Cycles*, 18, <https://doi.org/10.1029/2004GB002238>, 2004.
- 570 Bastviken, D., Sundgren, I., Natchimuthu, S., Reyier, H., and Gålfalk, M.: Cost-efficient approaches to
571 measure carbon dioxide (CO₂) fluxes and concentrations in terrestrial and aquatic
572 environments using mini loggers, *Biogeosciences*, 12, 3849–3859,
573 <https://doi.org/10.5194/bg-12-3849-2015>, 2015.
- 574 Beckebanze, L., Runkle, B.R.K., Walz, J., Wille, C., Holl, D., Helbig, M., Boike, J., Sachs, T., and
575 Kutzbach, L.: Lateral carbon export has low impact on the net ecosystem carbon balance of a
576 polygonal tundra catchment, *Biogeosciences*, 19, 3863–3876, <https://doi.org/10.5194/bg-19-3863-2022>, 2022.
- 578 Borge, A.F., Westermann, S., Solheim, I., and Etzelmüller, B.: Strong degradation of palsas and peat
579 plateaus in northern Norway during the last 60 years, *Cryosphere*, 11, 1–16,
580 <https://doi.org/10.5194/tc-11-1-2017>, 2017.
- 581 Boudreau, B.P., and Ruddick, B.R.: On a reactive continuum representation of organic matter
582 diagenesis, *Am. J. Sci.*, 291, 507–538, 1991.
- 583 Campeau, A., and Del Giorgio, P.A.: Patterns in CH₄ and CO₂ concentrations across boreal rivers:
584 Major drivers and implications for fluvial greenhouse emissions under climate change
585 scenarios, *Glob. Chang. Biol.*, 20, 1075–1088, <https://doi.org/10.1111/gcb.12479>, 2014.
- 586 Catalán, N., Marcé, R., Kothawala, D.N., and Tranvik, L.J.: Organic carbon decomposition rates
587 controlled by water retention time across inland waters, *Nat. Geosci.*, 9, 501–504,
588 <https://doi.org/10.1038/ngeo2720>, 2016.
- 589 Clayer, F., Gobeil, C., and Tessier, A.: Rates and pathways of sedimentary organic matter
590 mineralization in two basins of a boreal lake: Emphasis on methanogenesis and
591 methanotrophy, *Limnol. Oceanogr.*, 61, S1, <https://doi.org/10.1002/lno.10323>, 2016.
- 592 Crevecoeur, S., Vincent, W.F., Comte, J., Matveev, A., and Lovejoy, C.: Diversity and potential activity
593 of methanotrophs in high methane-emitting permafrost thaw ponds, *PLoS ONE*, 12,
594 e0188223, <https://doi.org/10.1371/journal.pone.0188223>, 2017.
- 595 Cui, S., Liu, P., Guo, H., Nielsen, C.K., Pullens, J.W.M., Chen, Q., Pugliese, L., and Wu, S.: Wetland
596 hydrological dynamics and methane emissions, *Commun. Earth Environ.*, 5, 1,
597 <https://doi.org/10.1038/s43247-024-01635-w>, 2024.
- 598 Gislén, K., Etzelmüller, B., Lussana, C., Hjort, J., Sannel, A.B.K., Isaksen, K., Westermann, S., Kuhry, P.,
599 Christiansen, H.H., Frampton, A., and Åkerman, J.: Permafrost Map for Norway, Sweden, and
600 Finland, *Permafrost Periglacial Process.*, 28, 359–378, <https://doi.org/10.1002/ppp.1922>, 2017.
- 601 Holgersson, M.A. and Raymond, P.A.: Large contribution to inland water CO₂ and CH₄ emissions from
602 very small ponds, *Nat. Geosci.*, 9, 222–226, <https://doi.org/10.1038/ngeo2654>, 2016.
- 603



- 604 Holmes, M.E., Crill, P.M., Burnett, W.C., McCalley, C.K., Wilson, R.M., Frohling, S., Chang, K.Y., Riley,
605 W.J., Varner, R.K., Hodgkins, S.B., McNichol, A.P., Saleska, S.R., Rich, V.I., and Chanton, J.P.:
606 Carbon Accumulation, Flux, and Fate in Stordalen Mire, a Permafrost Peatland in Transition,
607 *Glob. Biogeochem. Cycles*, 36, <https://doi.org/10.1029/2021GB007113>, 2022.
- 608 Hugelius, G., Loisel, J., Chadburn, S., Jackson, R.B., Jones, M., Macdonald, G., Marushchak, M.,
609 Olefeldt, D., Packalen, M., Siewert, M.B., Treat, C., Turetsky, M., Voigt, C., and Yu, Z.: Large
610 stocks of peatland carbon and nitrogen are vulnerable to permafrost thaw, *Proc. Natl. Acad.*
611 *Sci. U.S.A.*, 117, 20438–20446, <https://doi.org/10.1073/pnas.1916387117>, 2020.
- 612 Hugelius, G., Strauss, J., Zubrzycki, S., Harden, J.W., Schuur, E.A.G., Ping, C.L., Schirmermeister, L.,
613 Grosse, G., Michaelson, G.J., Koven, C.D., O'Donnell, J.A., Elberling, B., Mishra, U., Camill, P.,
614 Yu, Z., Palmtag, J., and Kuhry, P.: Estimated stocks of circumpolar permafrost carbon with
615 quantified uncertainty ranges and identified data gaps, *Biogeosciences*, 11, 6573–6593,
616 <https://doi.org/10.5194/bg-11-6573-2014>, 2014.
- 617 In 't Zandt, M.H., Liebner, S., and Welte, C.U.: Roles of Thermokarst Lakes in a Warming World,
618 *Trends Microbiol.*, 28, 769–779, <https://doi.org/10.1016/j.tim.2020.04.002>, 2020.
- 619 Kankaala, P., Huotari, J., Tulonen, T., and Ojala, A.: Lake-size dependent physical forcing drives
620 carbon dioxide and methane effluxes from lakes in a boreal landscape, *Limnol. Oceanogr.*,
621 58, 1915–1930, <https://doi.org/10.4319/lo.2013.58.6.1915>, 2013.
- 622 Kjellman, S.E., Axelsson, P.E., Etzelmüller, B., Westermann, S., and Sannel, A.B.K.: Holocene
623 development of subarctic permafrost peatlands in Finnmark, northern Norway, *Holocene*,
624 28, 1855–1869, <https://doi.org/10.1177/0959683618798126>, 2018.
- 625 Kjær, S.T., Westermann, S., Nedkvitne, N., and Dörsch, P.: Carbon degradation and mobilisation
626 potentials of thawing permafrost peatlands in northern Norway inferred from laboratory
627 incubations, *Biogeosciences*, 21, 4723–4737, <https://doi.org/10.5194/bg-21-4723-2024>,
628 2024.
- 629 Krutskikh, N., Ryazantsev, P., Ignashov, P., and Kabonen, A.: The Spatial Analysis of Vegetation Cover
630 and Permafrost Degradation for a Subarctic Palsa Mire Based on UAS Photogrammetry and
631 GPR Data in the Kola Peninsula, *Remote Sens.*, 15, 1896,
632 <https://doi.org/10.3390/rs15071896>, 2023.
- 633 Krüger, J.P., Conen, F., Leifeld, J., and Alewell, C.: Palsa Uplift Identified by Stable Isotope Depth
634 Profiles and Relation of $\delta^{15}\text{N}$ to C/N Ratio, *Permafrost Periglac. Process.*, 28, 485–492,
635 <https://doi.org/10.1002/ppp.1936>, 2017.
- 636 Kuhn, M., Lundin, E.J., Giesler, R., Johansson, M., and Karlsson, J.: Emissions from thaw ponds largely
637 offset the carbon sink of northern permafrost wetlands, *Sci. Rep.*, 8,
638 <https://doi.org/10.1038/s41598-018-27770-x>, 2018.
- 639 Laurion, I., Massicotte, P., Mazoyer, F., Negandhi, K., and Mladenov, N.: Weak mineralization despite
640 strong processing of dissolved organic matter in Eastern Arctic tundra ponds, *Limnol.*
641 *Oceanogr.*, 66, <https://doi.org/10.1002/lno.11634>, 2020.
- 642 Leppiniemi, O., Karjalainen, O., Aalto, J., Luoto, M., and Hjort, J.: Environmental spaces for palsas and
643 peat plateaus are disappearing at a circumpolar scale, *Cryosphere*, 17, 3157–3176,
644 <https://doi.org/10.5194/tc-17-3157-2023>, 2023.
- 645 Lundin, E.J., Giesler, R., Persson, A., Thompson, M.S., and Karlsson, J.: Integrating carbon emissions
646 from lakes and streams in a subarctic catchment, *J. Geophys. Res.-Biogeosci.*, 118, 1200–
647 1207, <https://doi.org/10.1002/jgrg.20092>, 2013.
- 648 Martin, L.C.P., Nitzbon, J., Scheer, J., Aas, K.S., Eiken, T., Langer, M., Filhol, S., Etzelmüller, B., and
649 Westermann, S.: Lateral thermokarst patterns in permafrost peat plateaus in northern
650 Norway, *Cryosphere*, 15, 3423–3442, <https://doi.org/10.5194/tc-15-3423-2021>, 2021.
- 651 Martin, L.C.P., Nitzbon, J., Aas, K.S., Etzelmüller, B., Kristiansen, H., and Westermann, S.: Stability
652 Conditions of Peat Plateaus and Palsas in Northern Norway, *J. Geophys. Res.-Earth Surf.*,
653 124, 705–719, <https://doi.org/10.1029/2018JF004945>, 2019.



- 654 Matveev, A., Laurion, I., and Vincent, W.F.: Methane and carbon dioxide emissions from thermokarst
655 lakes on mineral soils, *Arct. Sci.*, 4, 584–604, <https://doi.org/10.1139/as-2017-0047>, 2018.
- 656 Mostovaya, A., Hawkes, J.A., Dittmar, T., and Tranvik, L.J.: Molecular Determinants of Dissolved
657 Organic Matter Reactivity in Lake Water, *Frontiers in Earth Science*, 5,
658 <https://doi.org/10.3389/feart.2017.00106>, 2017.
- 659 Muster, S., Riley, W.J., Roth, K., Langer, M., Cresto Aleina, F., Koven, C.D., Lange, S., Bartsch, A.,
660 Grosse, G., Wilson, C.J., Jones, B.M., and Boike, J.: Size Distributions of Arctic Waterbodies
661 Reveal Consistent Relations in Their Statistical Moments in Space and Time, *Frontiers in*
662 *Earth Science*, 7, <https://doi.org/10.3389/feart.2019.00005>, 2019.
- 663 Muster, S., Roth, K., Langer, M., Lange, S., Cresto Aleina, F., Bartsch, A., Morgenstern, A., Grosse, G.,
664 Jones, B., Sannel, A.B.K., Sjöberg, Y., Günther, F., Andresen, C., Veremeeva, A., Lindgren,
665 P.R., Bouchard, F., Lara, M.J., Fortier, D., Charbonneau, S., Virtanen, T.A., Hugelius, G.,
666 Palmtag, J., Siewert, M.B., Riley, W.J., Koven, C.D., and Boike, J.: PeRL: A Circum-Arctic
667 Permafrost Region Pond and Lake Database, *Earth System Science Data*, 9, 317–348,
668 <https://doi.org/10.5194/essd-9-317-2017>, 2017.
- 669 Olefeldt, D., Heffernan, L., Jones, M.C., Sannel, A.B.K., Treat, C.C., Turetsky, M.R.: Permafrost Thaw in
670 Northern Peatlands: Rapid Changes in Ecosystem and Landscape Functions. In: Canadell, J.G.,
671 Jackson, R.B. (eds) *Ecosystem Collapse and Climate Change*. Ecological Studies, vol 241.
672 Springer, Cham. https://doi.org/10.1007/978-3-030-71330-0_3, 2021.
- 673 Payette, S., Delwaide, A., Caccianiga, M., and Beauchemin, M.: Accelerated Thawing of Subarctic
674 Peatland Permafrost over the Last 50 Years, *Geophysical Research Letters*, 31, 18,
675 <https://doi.org/10.1029/2004GL020358>, 2004.
- 676 Peura, S., Wauthy, M., Simone, D., Eiler, A., Einarsdóttir, K., Rautio, M., and Bertilsson, S.: Ontogenic
677 Succession of Thermokarst Thaw Ponds Is Linked to Dissolved Organic Matter Quality and
678 Microbial Degradation Potential, *Limnology and Oceanography*, 65(S1),
679 <https://doi.org/10.1002/lno.11349>, 2019.
- 680 Pirk, N., Aalstad, K., Mannerfelt, E.S., Clayer, F., de Wit, H., Christiansen, C.T., Althuizen, I., Lee, H.,
681 and Westermann, S.: Disaggregating the Carbon Exchange of Degrading Permafrost
682 Peatlands Using Bayesian Deep Learning, *Geophysical Research Letters*, 51, 10,
683 <https://doi.org/10.1029/2024GL109283>, 2024.
- 684 Polishchuk, Y.M., Bogdanov, A.N., Muratov, I.N., Polishchuk, V.Y., Lim, A., Manasypov, R.M.,
685 Shirokova, L.S., and Pokrovsky, O.S.: Minor Contribution of Small Thaw Ponds to the Pools of
686 Carbon and Methane in the Inland Waters of the Permafrost-Affected Part of the Western
687 Siberian Lowland, *Environmental Research Letters*, 13, 4, [https://doi.org/10.1088/1748-](https://doi.org/10.1088/1748-9326/aab046)
688 [9326/aab046](https://doi.org/10.1088/1748-9326/aab046), 2018.
- 689 Raymond, P.A., Hartmann, J., Lauerwald, R., Sobek, S., McDonald, C., Hoover, M., Butman, D., Striegl,
690 R., Mayorga, E., Humborg, C., Kortelainen, P., Dürr, H., Meybeck, M., Ciais, P., and Guth, P.:
691 Global Carbon Dioxide Emissions from Inland Waters, *Nature*, 503, 7476, 355–359,
692 <https://doi.org/10.1038/nature12760>, 2013.
- 693 R Core Team: R: A Language and Environment for Statistical Computing, R Foundation for Statistical
694 Computing, Vienna, Austria, <https://www.R-project.org/>, 2021.
- 695 Sannel, A.B.K., and Kuhry, P.: Warming-Induced Destabilization of Peat Plateau/Thermokarst Lake
696 Complexes, *Journal of Geophysical Research: Biogeosciences*, 116, G3,
697 <https://doi.org/10.1029/2010JG001635>, 2011.
- 698 Schelker, J., Singer, G.A., Ulseth, A.J., Hengsberger, S., and Battin, T.J.: CO₂ Evasion from a Steep,
699 High Gradient Stream Network: Importance of Seasonal and Diurnal Variation in Aquatic
700 pCO₂ and Gas Transfer, *Limnology and Oceanography*, 61, 5, 1826–1838,
701 <https://doi.org/10.1002/lno.10339>, 2016.
- 702 Schuur, E.A.G., Bockheim, J., Canadell, J.G., Euskirchen, E., Field, C.B., Goryachkin, S.V., Hagemann,
703 S., Kuhry, P., Lafleur, P.M., Lee, H., Mazhitova, G., Nelson, F.E., Rinke, A., Romanovsky, V.E.,
704 Shiklomanov, N., Tarnocai, C., Venevsky, S., Vogel, J.G., and Zimov, S.A.: Vulnerability of



- 705 Permafrost Carbon to Climate Change: Implications for the Global Carbon Cycle, *Bioscience*,
706 58, 8, 701–714, <https://doi.org/10.1641/B580807>, 2008.
- 707 Schuur, E.A.G., McGuire, A.D., Schädel, C., Grosse, G., Harden, J.W., Hayes, D.J., Hugelius, G., Koven,
708 C.D., Kuhry, P., Lawrence, D.M., Natali, S.M., Olefeldt, D., Romanovsky, V.E., Schaefer, K.,
709 Turetsky, M.R., Treat, C.C., and Vonk, J.E.: Climate Change and the Permafrost Carbon
710 Feedback, *Nature*, 520, 7546, 171–179, <https://doi.org/10.1038/nature14338>, 2015.
- 711 SeNorge: Norges vassdrags- og energidirektorat, Norsk: <https://www.senorge.no/>, last access 22
712 November 2024.
- 713 Shirokova, L. S., Chupakov, A. V., Zabelina, S. A., Neverova, N. V., Payandi-Rolland, D., Causserand, C.,
714 Karlsson, J., and Pokrovsky, O. S.: Humic surface waters of frozen peat bogs (permafrost
715 zone) are highly resistant to bio- and photodegradation, *Biogeosciences*, 16(12), 2511–2526,
716 <https://doi.org/10.5194/bg-16-2511-2019>, 2019.
- 717 Shirokova, L. S., Pokrovsky, O. S., Kirpotin, S. N., Desmukh, C., Pokrovsky, B. G., Audry, S., and Viers,
718 J.: Biogeochemistry of organic carbon, CO₂, CH₄, and trace elements in thermokarst water
719 bodies in discontinuous permafrost zones of Western Siberia, *Biogeochemistry*, 113(1–3),
720 573–593, <https://doi.org/10.1007/s10533-012-9790-4>, 2012.
- 721 Sim, T. G., Swindles, G. T., Morris, P. J., Baird, A. J., Cooper, C. L., Gallego-Sala, A. V., Charman, D. J.,
722 Roland, T. P., Borken, W., Mullan, D. J., Aquino-López, M. A., and Gałka, M.: Divergent
723 responses of permafrost peatlands to recent climate change, *Environ. Res. Lett.*, 16(3),
724 035003, <https://doi.org/10.1088/1748-9326/abe00b>, 2021.
- 725 Sollid, J. L., Andersen, S., Hamre, N., Kjeldsen, O., Salvigsen, O., Sturød, S., Tveitå, T., and
726 Wilhelmsen, A.: Deglaciation of Finnmark, North Norway, *Norsk Geografisk Tidsskr.*, 27(4),
727 233–325, <https://doi.org/10.1080/00291957308551960>, 1973.
- 728 Stumm, W. and Morgan, J.J.: *Aquatic chemistry: chemical equilibria and rates in natural waters*. John
729 Wiley & Sons, 2013.
- 730 Swindles, G. T., Morris, P. J., Mullan, D., Watson, E. J., Turner, T. E., Roland, T. P., Amesbury, M. J.,
731 Kokfelt, U., Schoning, K., Pratte, S., Gallego-Sala, A., Charman, D. J., Sanderson, N., Garneau,
732 M., Carrivick, J. L., Woulds, C., Holden, J., Parry, L., and Galloway, J. M.: The long-term fate of
733 permafrost peatlands under rapid climate warming, *Sci. Rep.*, 5, 17951,
734 <https://doi.org/10.1038/srep17951>, 2015.
- 735 Tank, S. E., Fellman, J. B., Hood, E., and Kritzberg, E. S.: Beyond respiration: Controls on lateral
736 carbon fluxes across the terrestrial–aquatic interface, *Limnol. Oceanogr. Lett.*, 3(3), 76–88,
737 <https://doi.org/10.1002/lol2.10068>, 2018.
- 738 Thrane, J.-E., de Wit, H., Blakseth, T.A., Skancke, L.B. and Garmo, Ø.A.: Correcting for bias in
739 freshwater total nitrogen concentrations obtained with a modified standard (NS4743)
740 method. NIVA-rapport, 2020.
- 741 Turetsky, M. R., Abbott, B. W., Jones, M. C., Anthony, K. W., Olefeldt, D., Schuur, E. A. G., Grosse, G.,
742 Kuhry, P., Hugelius, G., Koven, C., Lawrence, D. M., Gibson, C., Sannel, A. B. K., and McGuire,
743 A. D.: Carbon release through abrupt permafrost thaw, *Nat. Geosci.*, 13(2), 138–143,
744 <https://doi.org/10.1038/s41561-019-0526-0>, 2020.
- 745 Valiente, N., Eiler, A., Alleson, L., Andersen, T., Clayer, F., Crapart, C., Dörsch, P., Fontaine, L.,
746 Heuschele, J., Vogt, R. D., Wei, J., de Wit, H. A., and Hessen, D. O.: Catchment properties as
747 predictors of greenhouse gas concentrations across a gradient of boreal lakes, *Front.*
748 *Environ. Sci.*, 10, <https://doi.org/10.3389/fenvs.2022.880619>, 2022.
- 749 Verdonen, M., Störmer, A., Lotsari, E., Korpelainen, P., Burkhard, B., Colpaert, A., and Kumpula, T.:
750 Permafrost degradation at two monitored palsamires in north-west Finland, *The*
751 *Cryosphere*, 17, 1803–1819, <https://doi.org/10.5194/tc-17-1803-2023>, 2023.
- 752 Vigneron, A., Cruaud, P., Bhiry, N., Lovejoy, C., and Vincent, W. F.: Microbial community structure
753 and methane cycling potential along a thermokarst pond-peatland continuum,
754 *Microorganisms*, 7, 1–16, <https://doi.org/10.3390/microorganisms7110486>, 2019.



- 755 Vogt, R.D. and Skancke, L.B.: Overvåking av langtransportert forurenset luft og nedbør. Årsrapport–
756 Vannkjemiske effekter 2021. NIVA report 7778-2022; Miljødirektoratet report 2347-2022,
757 2022.
- 758 Vonk, J. E., Tank, S. E., Bowden, W. B., Laurion, I., Vincent, W. F., Alekseychik, P., Amyot, M., Billet,
759 M. F., Canário, J., Cory, R. M., Deshpande, B. N., Helbig, M., Jammet, M., Karlsson, J.,
760 Larouche, J., MacMillan, G., Rautio, M., Walter Anthony, K. M., and Wickland, K. P.: Reviews
761 and syntheses: Effects of permafrost thaw on Arctic aquatic ecosystems, *Biogeosciences*, 12,
762 7129–7167, <https://doi.org/10.5194/bg-12-7129-2015>, 2015.
- 763 Vähätalo, A. V., Aarnos, H., and Mäntyniemi, S.: Biodegradability continuum and biodegradation
764 kinetics of natural organic matter described by the beta distribution, *Biogeochemistry*, 100,
765 227–240, <https://doi.org/10.1007/s10533-010-9419-4>, 2010.
- 766 Wallin, M. B., Campeau, A., Audet, J., Bastviken, D., Bishop, K., Kocic, J., Laudon, H., Lundin, E.,
767 Löfgren, S., Natchimuthu, S., Sobek, S., Teutschbein, C., Weyhenmeyer, G. A., and Grabs, T.:
768 Carbon dioxide and methane emissions of Swedish low-order streams: A national estimate
769 and lessons learnt from more than a decade of observations, *Limnol. Oceanogr. Lett.*, 3,
770 156–167, <https://doi.org/10.1002/lo2.10061>, 2018.
- 771 Walter, K. M., Chanton, J. P., Chapin, F. S. III, Schuur, E. A. G., and Zimov, S. A.: Methane production
772 and bubble emissions from arctic lakes: Isotopic implications for source pathways and ages,
773 *J. Geophys. Res.-Biogeosci.*, 113, G03001, <https://doi.org/10.1029/2007JG000569>, 2008.
- 774 Walter, K. M., Zimov, S. A., Chanton, J. P., Verbyla, D., and Chapin, F. S.: Methane bubbling from
775 Siberian thaw lakes as a positive feedback to climate warming, *Nature*, 443, 71–75,
776 <https://doi.org/10.1038/nature05040>, 2006.
- 777 Ward, C. P., and Cory, R. M.: Chemical composition of dissolved organic matter draining permafrost
778 soils, *Geochim. Cosmochim. Acta*, 167, 63–79, <https://doi.org/10.1016/j.gca.2015.07.001>,
779 2015.
- 780 Westrich, J. T., and Berner, R. A.: The role of sedimentary organic matter in bacterial sulfate
781 reduction: The G model tested, *Limnol. Oceanogr.*, 29, 236–249,
782 <https://doi.org/10.4319/lo.1984.29.2.0236>, 1984.
- 783 Wickham, H.: *ggplot2: Elegant Graphics for Data Analysis*, Springer-Verlag New York, ISBN 978-3-
784 319-24277-4, <https://ggplot2.tidyverse.org>, 2016.
- 785 Wik, M., Varner, R. K., Anthony, K. W., MacIntyre, S., and Bastviken, D.: Climate-sensitive northern
786 lakes and ponds are critical components of methane release, *Nat. Geosci.*, 9, 99–105,
787 <https://doi.org/10.1038/ngeo2578>, 2016.
- 788 Wilhelm, E., Battino, R., and Wilcock, R. J.: Low-pressure solubility of gases in liquid water, *Chem.*
789 *Rev.*, 77, 219–262, <https://doi.org/10.1021/cr60306a003>, 1977.
- 790 Yang, H., Andersen, T., Dörsch, P., Tominaga, K., Thrane, J.-E., and Hessen, D. O.: Greenhouse gas
791 metabolism in Nordic boreal lakes, *Biogeochemistry*, 126, 211–225,
792 <https://doi.org/10.1007/s10533-015-0154-8>, 2015.
- 793 Zimov, S. A., Davydov, S. P., Zimova, G. M., Davydova, A. I., Schuur, E. A. G., Dutta, K., and Chapin, F.
794 S. III: Permafrost carbon: Stock and decomposability of a globally significant carbon pool,
795 *Geophys. Res. Lett.*, 33, L20502, <https://doi.org/10.1029/2006GL027484>, 2006.
- 796 Zolkos, S., and Tank, S. E.: Experimental evidence that permafrost thaw history and mineral
797 composition shape abiotic carbon cycling in thermokarst-affected stream networks, *Front.*
798 *Earth Sci.*, 8, 1–11, <https://doi.org/10.3389/feart.2020.00152>, 2020.
- 799 Zolkos, S., Tank, S. E., Striegl, R. G., and Kokelj, S. V.: Thermokarst effects on carbon dioxide and
800 methane fluxes in streams on the Peel Plateau (NWT, Canada), *J. Geophys. Res.-Biogeosci.*,
801 124, 1781–1798, <https://doi.org/10.1029/2019JG005038>, 2019.
- 802 Åberg, J., and Wallin, M. B.: Evaluating a fast headspace method for measuring DIC and subsequent
803 calculation of $p\text{CO}_2$ in freshwater systems, *Inland Waters*, 4, 157–166,
804 <https://doi.org/10.5268/IW-4.2.694>, 2014.